# Probing the potential of CdZnTe for high-energy high-flux 2D X-ray detection using the XIDer incremental digital integrating readout

Marin Collonge[1,2], Oriane Baussens[1], Paolo Busca[1]*,
Pablo Fajardo[1], Peter Fischer[2], Thierry Martin[1], Michael Ritzert[2],
Marie Ruat[1], David Schimansky[2] and Morag Williams[1]

[1]Detector and Electronics Group, European Synchrotron Radiation Facility, Grenoble, France, [2]Institut für Technische Informatik, Universität Heidelberg, Heidelberg, Germany

The latest synchrotron radiation sources have the capability to produce X-ray beams with a photon flux that can be up to three orders of magnitude higher than previous-generation facilities, and that are not manageable by the currently available 2D photon-counting pixel detectors. The construction of new detectors that exceed the limitations of existing devices is a critical strategic need. Developing such detectors is a challenge in terms of readout electronics as well as sensor material, particularly in the case of devices intended to operate at X-ray energies above 30 keV. The approach adopted at the ESRF to deal with this major difficulty is twofold: the use of a novel semiconductor material with improved electrical properties, high-flux CdZnTe, and the investigation of a specific readout scheme, incremental digital integration, via the XIDer project in collaboration with the University of Heidelberg. Incremental digital integration is a method intended to be less sensitive to variations of the dark current than the conventional charge integration readout. However, this readout scheme requires that the leakage current from the sensor material stays below a certain threshold to reduce the leakage contributions. This paper introduces the ESRF strategy and few examples of the methods employed to evaluate the performance and leakage current behavior of high-flux CdZnTe pixelated sensors. These examples illustrate the first results obtained with this material under moderate to very high X-ray irradiation fluxes of up to $10^{12}$ photons/mm$^2$/s.

# 1 Introduction

## 1.1 Exploiting 4<sup>th</sup> generation synchrotron sources: limitations of current detectors

The proper exploitation of the latest generation of synchrotron radiation storage rings presents non-trivial challenges. In addition to the increased brilliance of these very low emittance accelerator-based sources, the possibility of operating with reduced gap undulators and the use of more efficient optics allow the delivery of X-ray beams of unprecedented intensity [1]. The actual gain in photon flux over previous sources is highly dependent on the particular applications and experimental setups, but in many cases can be as much as two to three orders of magnitude [2]. The photon fluxes are expected to increase further with the development of optimized insertion devices and improved X-ray optics. In this scenario, the construction of new X-ray detectors that exceed the limits of current devices by several orders of magnitude is a critical strategic need. In the case of the EBS (Extremely Brilliant Source) [3], the new ESRF storage ring and the first fourth-generation high-energy synchrotron facility in operation, the monochromatic X-ray beams can reach $10^{16}$ photons per second. In addition, the challenge of building a new generation of detectors is further increased due to the need to cover a significant number of applications with photon energies at or above 30 keV.

The most suitable 2D detectors currently available for diffraction and scattering experiments at the ESRF and other synchrotron storage rings are hybrid pixel detectors, built with pixelated semiconductor sensors, and operating in photon-counting mode [4, 5]. Thanks to the direct conversion of X-rays into charge, these devices provide the single-photon sensitivity required for photon-counting operation. And the signal-processing scheme in a photon counting device produces output data with extremely low readout noise that can be negligible in most practical cases [6, 7]. Another, less obvious, but extremely important feature of photon-counting readout is the possibility of engineering signal-processing electronics that are insensitive to fluctuations of the dark current generated in the semiconductor sensor. This aspect, which is relevant for silicon-based devices, becomes absolutely critical when it comes to high-energy photon detectors built with pixelated compound semiconductors. It has been instrumental in the successful deployment of 2D photon-counting CdTe detectors at the ESRF, as well as at a number of high-energy experimental stations at other synchrotron radiation facilities [8–10].

However, although photon-counting hybrid pixel technology is the current state of the art for 2D detection in a wide range of synchrotron applications, the maximum photon flux per pixel is limited by pulse pile-up [11]. When the average photon flux per pixel approaches a certain X-ray hit rate, the pulse discrimination circuitry begins to miss counts and the detector suffers from count losses. In practice, with the most advanced current photon-counting detectors, when the flux per pixel approaches few million photon hits per second, the pile-up count losses exceed 10% of the average incident hit rate [8, 12]. This is a major limitation of existing detectors, which prevents the efficient use of new generation of synchrotrons. Two different strategies are being investigated at the ESRF and other facilities to overcome the above limitation: (i) the design of new photon-counting detectors with one to two orders of

magnitude higher count rate capability, (ii) the implementation of special charge-integrating detectors suitable for time-resolved experiments and able to operate with continuous beams at high photon energies at storage rings.

## 1.2 The need and challenge of building high-energy charge-integrating detectors

It is possible to increase the count rate capabilities of photon-counting detectors by developing faster front-end readout electronics with pile-up compensation techniques or other strategies such as reducing the pixel size to increase the number of counting channels per pixel area [13–15]. However, the maximum achievable photon flux with photon-counting devices would still not be sufficient for applications dealing with very strong signals, such as those found in many diffraction experiments in material science. In these experiments, the samples under study are usually made of inorganic materials and the diffraction signals at the detector can be very intense. The energy of the X-ray photons must be high enough to penetrate and properly probe the regions of the samples being investigated. This results in illuminated sample volumes that are usually well above 100 μm in size, which are significantly larger than in other types of diffraction or scattering experiments with thin samples as it is the case, for instance, when studying organic or biological materials. This circumstance strongly influences the minimum required pixel size as, although the spatial distribution of the measured pattern is dependent on the distance from the sample to the active plane of the detector, the highest spatial resolution of the pattern is limited, among other parameters, by the size of the illuminated volume in the sample which is indeed the effective diffracting source. This consideration is not applicable to coherent scattering experiments, but it is fully valid for conventional diffraction techniques such as single-crystal or powder diffraction and has as a consequence that the required detector pixel size for this type of experiments is not very small. In practice, in most material science experiments, a pixel size in the range of 100 μm–200 μm is well adapted to properly record the diffraction patterns that can be very intense, reaching, or exceeding in some cases, $10^9$ photons per second per pixel.

The photon statistics in experiments with such intense signals are sufficient to investigate physical phenomena on the micro- and sub-microsecond time scale, including irreversible processes. Such short time domains, that were unattainable with the previous generation of synchrotron sources, can be reached with detectors able to sample the diffraction patterns at MHz rates while coping with the high incident photon flux. This requirement corresponds quite closely to the capabilities of the high dynamic range charge-integrating hybrid pixel detectors developed over the last decade for free-electron lasers [16, 17] and more recently for spectroscopy applications [18]. These detectors are designed to operate by integrating the charge coming from the pixelated sensors during a very short time window for which the undesired signal component resulting from the integration of the sensor leakage current is negligible. Although these last generation X-ray integrating detectors are very well suited for very intense single pulse measurements or short integration times, they do not offer the versatility required for applications at storage rings, in which the duration of the integration intervals, the acquisition duty cycle and the operation conditions vary considerably from experiment to experiment.

Furthermore, the use of high-Z compound semiconductor sensor materials, which is essential to ensure good absorption efficiency above 30 keV, results in the degradation of the performance of detector systems due to charge trapping and to the associated polarization effects [19]. The polarization effects correspond to over-time changes in the electric field distribution in the sensor due to charge build-up. The build-up can be caused both by the bias applied to the sensor and by high incident X-ray doses. The bias-induced polarization effect specifically affects Schottky devices by screening the electric field near the cathode [20]. This not only results in a reduction of the charge collection efficiency, but also in a reduction of the Schottky barrier height, which causes the leakage current in the sensor to increase. Moreover, the bias-induced polarization effect can take up to hours to stabilize, which means that leakage current is unstable during that time. High and unstable values of leakage current make it challenging to implement an effective leakage current compensation scheme. And without a proper compensation, the leakage current is integrated along with the signal of interest. For intermediate or long integration times, the leakage dominates the signal of interest, thus degrading the dynamic range of the integrating system. As for the irradiation-induced polarization, it affects both ohmic and Schottky devices [21]. This effect depends on many factors, including the energy and intensity of the X-ray beam, the sensor type and the temperature. Like in the case of bias-induced polarization, the charge build-up created can screen the electric field in the sensor and hinder charge collection. Moreover, since in this case the charge build-up is tied to the irradiation, stopping the irradiation leads to the detrapping of the built-up charge. This results in a residual current, the aftersignal, that decreases over time with characteristic time constants linked to the traps levels implicated in the initial build-up. This aftersignal component, also referred to as "afterglow" or "lag" in the literature [22–24], is particularly detrimental for applications requiring pulsed irradiation. In the case of semiconductor compounds of the CdTe family, the polarization effect is caused by the very poor charge transport properties of holes and it makes conventional charge-integration readout schemes inapplicable in practice.

## 1.3 An ESRF approach to mitigate the leakage current contributions

As introduced in the previous section, a major challenge faced when building high-energy charge-integrating detectors for storage rings is finding a sufficiently effective method to reduce the contributions of the leakage current from the sensor material. The approach adopted follows two complementary paths. On the one side, there is the use of a semiconductor material with improved electrical properties and minimum leakage current variations: the so called high-flux CdZnTe (HF-CZT) [25, 26]. On the other side, the implementation of a specific readout scheme, the incremental digital integration, which uses quantization in the signal conversion process to partially cancel undesired contributions coming from the integration of the sensor leakage current. The investigation of incremental digital integration is a central part of the XIDer project, a collaboration of the ESRF and the University of Heidelberg, and has been described and discussed in previous

publications [27, 28]. The results presented in this work are examples of the approach followed at ESRF for the evaluation of the behavior of HF-CZT sensors at high X-ray incident fluxes with both standalone discrete devices and with pixelated sensors hybridized with XIDer readout ASICs.

## 2 Materials and methods

### 2.1 High-Z sensors and hybrids

HF-CZT material is a specific variant of CdZnTe, produced by Redlen Technologies [29], that has the particularity of presenting significantly enhanced hole transport properties compared to more conventional spectroscopic CZT and to CdTe [25, 26]. Thanks to this particularity, HF-CZT is much less subject to the build-up of positive space charge in the sensor volume and therefore less sensitive to both the bias-driven and radiation-driven polarization phenomena. Previous work has shown that, at 20 keV, HF-CZT is indeed more resilient than its standard counterpart, at least up to $10^{10}$ ph/mm$^2$/s [30, 31]. Although the material used in this work was grown by Redlen Technologies, the samples under study were reprocessed by IMEM-CNR with their own contact technology and diced to produce sensors with the desired size and electrode layout. All the sensors are terminated with quasi-ohmic contacts at both sides and have a continuous cathode and a structured anode. The anodes are made of sputtered platinum electrodes with layouts that include pixelated structures surrounded by a full metal contact that is used as a guard ring. For operation, the cathodes of the sensors are biased to negative voltages while the guard rings are grounded and the pixel contacts at the anodes are connected to the measurement devices.

This work presents results obtained with two types of HF-CZT sensors: standalone samples measured with discrete readout electronics, and devices that were hybridized with the XIDer readout ASICs.

The standalone samples studied in this paper are 1.5 mm thick and have a total external size, after reprocessing, of approximately 5 × 5 mm$^2$. The anode layout, as seen in Figure 1, includes two single pixels and a 2 × 2 pixel matrix surrounded by the full guard ring contact. All the pixels are 500 μm square. On the cathode side, sample 1 has a gold electrode while sample 2 has a platinum electrode. These electrodes were manufactured via electroless and sputtering processes, respectively. The samples were mounted onto PCBs with bicomponent epoxy glue and bonded using copper wires and conductive silver epoxy (Figure 1). These samples were originally part of a larger study, testing all possible electrode configurations with gold and platinum [32]. In this previous study, it was found that a platinum electrode is needed on the anode (Cd-face) to act as a hole blocking layer, but that both gold and platinum act as electron blocking layers on the cathode (Te-face). Essentially, both samples discussed in the present study exhibited similar response under dark conditions. In addition, the response of these samples under irradiation has previously been published [31] for lower incident X-ray fluxes than those presented in this paper. It was found that both samples gave similar responses under irradiation.

In the current paper, all of the measurements presented were performed, at room temperature, on the single pixels. During measurements of each sample, they were placed in a custom-
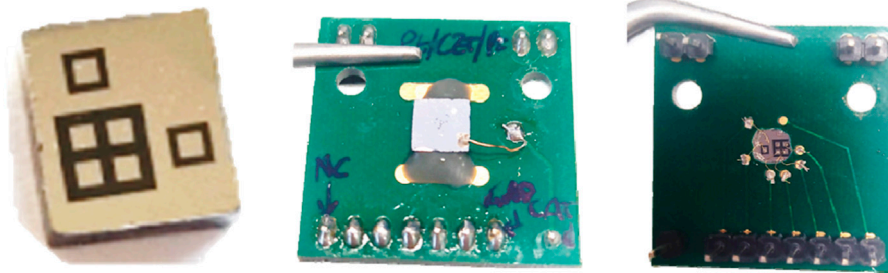
**FIGURE 1**
Standalone HF-CZT samples: Electrode layout and pictures of one of the samples mounted on the test PCB. [left] Pixelated anode layout. [center] Top side of the test PCB. [right] Bottom side of the test PCB.
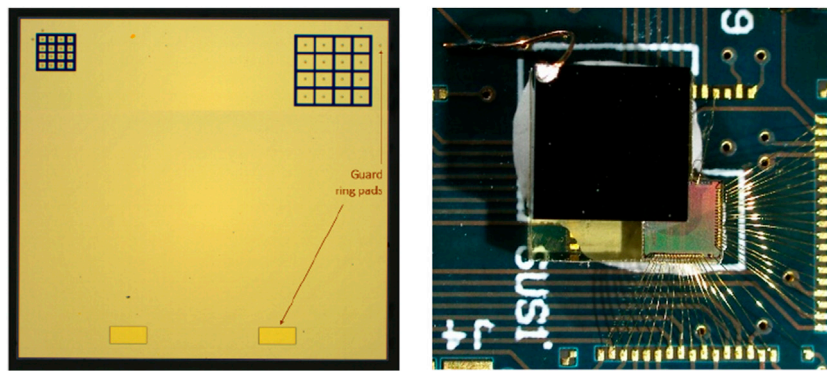


**FIGURE 2**
Hybridized HF-CZT devices: [left] 4 × 4 mm$^2$ sensor before hybridization, showing the 100 μm and 200 μm pitch 16-pixel matrices designed to be bonded to XIDer ASICs. [right] Picture of the 200 μm pitch sensor-ASIC assembly mounted on the test PCB.

made metal box with a Kapton tape entrance window and their cathodes were biased at −1000 V (6.7 kV/cm) using a high voltage power supply ISEG SHQ 224. The current collected by the single pixel was then measured using a picoammeter Keithley 6,485.

The devices with integrated readout are assemblies built with small HF-CZT pixelated sensors hybridized to XIDer readout ASICs. These readout chips are designed in CMOS 65 nm TSMC technology and implement the incremental digital integration readout [27, 28]. The HF-CZT sensors are 2 mm thick in this case and include two 4 × 4 pixel minimatrices of 100 μm and 200 μm pitch, as shown in the picture at the left of Figure 2. The cathode consists of a continuous platinum contact. In the assemblies used for this work only the 200 μm minimatrix was connected to the 16-channel readout ASIC. The bonding was performed by Polymer Assembly Technology [33] by applying a low-temperature flip-chip process with gold studs and conductive epoxy [34]. The picture on the right shows one of the hybridized assemblies mounted on the test PCB with the connection to the top cathode electrode that, in operation, was biased at −1000 V.

For comparison purposes, the results obtained with the HF-CZT hybrids are presented in the next section together with results obtained with CdTe sensors from the company Acrorad [35]. These sensors are also terminated with ohmic platinum contacts, at both the anode and the cathode, and have the same size and layout

that is depicted in Figure 2. However, as the CdTe sensors are 1 mm thick, thinner than the HF-CZT devices, they were biased at a proportionally lower voltage of −500 V to operate with a comparable internal electric field.

Note that the electric fields used to characterize the standalone samples (6.7 kV/cm) and the hybridized samples (5 kV/cm) are different. This difference comes from the fact that the measurements were planned separately for each type of samples. However, in both cases, the electric field was chosen to ensure that the samples were operated in full charge-collection regime. This regime occurs around 1 kV/cm for both CZT and CdTe samples.

## 2.2 Application of the incremental digital integration readout

The basic principle of incremental digital integration is the division of the total exposure time in a number N of subintervals, subframes in the XIDer terminology, where for each subframe the input signal in each pixel is integrated and digitized [27]. The resulting pixel intensity is the sum of the N digital values produced during the total integration time, an operation that is fully performed by the pixel electronics in the readout chip. This scheme, operating with very short subframes in the micro- or sub-

microsecond range, implements an in-pixel fast analog-to-digital conversion with a certain level of rejection of the dark current contribution. The rejection is effective if the total leakage charge collected during each subframe is well below a certain threshold that, in the case of the XIDer circuit implementation, is determined by the resolution of the analog-to-digital converter (ADC). When working with monochromatic radiation, the least significant bit of the ADC in the pixel is typically set to the equivalent of one X-ray photon and the threshold to 50% of that value. For example, with 30 keV monochromatic irradiation, the discrimination threshold would be set at an equivalent 15 keV, which in CdZnTe corresponds to a constant 260 pA/pixel leakage current being integrated during a 2 μs window. The incremental digital integration readout then behaves at low photon fluxes like a photon-counting readout, and at higher photon fluxes, when quantization error becomes negligible, digital integration is functionally equivalent to a conventional charge-integrating scheme [36].

In the work presented in this paper, the XIDer readout ASIC was used as a tool to investigate the variation of the leakage current of the HF-CZT devices in the microsecond scale. For this purpose, the devices were calibrated to operate with 30 keV photons, the lowest photon energy they were designed to handle, and configured to acquire single subframes. The calibration is an important step which consists in trimming four adjustable parameters of the internal circuitry of the ASIC on a per-pixel basis. This includes the trimming of the quantization steps and the discrimination thresholds with respect to the energy of the incident photons in the pixel front-end electronics, for each of the two pipelined stages, coarse and fine [28]. The calibration procedure relies on the internal charge injection circuitry and each parameter was trimmed by analyzing the effect of a sweep of their respective DAC in the chip, under the injection of a specific amount of charge, *e.g.*, the charge equivalent to the integration of one 30 keV photon. The equivalence between photon energy and injected charge was derived from the theoretical sensor average ionizing energy, 4.64 eV per electron-hole pair for CZT [37], and the nominal values of the injection circuitry components. Discussing the procedure in more detail is beyond the scope of this paper but it is relevant to point out that, although the absolute calibration accuracy is limited by the manufacturing tolerance of the charge injection circuitry, it is possible and important to check the consistency of the trimming of the four internal parameters in each pixel. The proper relative matching of the pixel values can be assessed by using the charge injector itself as any deviation in the response of the front-end electronics reveals mismatches in the calibration of the coarse and fine stages. For that purpose, any arbitrary but controlled signal distribution can be injected into the front-end to verify the correspondence of the data produced by the ASIC. In the example below, a waveform generator was used to inject a signal corresponding to a predefined number of 30 keV photons with a superimposed Gaussian random component. For each number of equivalent photons, a large number of subframes was acquired, with the amplitude of the noise-like component adjusted to make the injection approximately match the signal distribution that would be produced by a Poissonian X-ray source illuminating uniformly the device. Examples of retrieved distributions of the acquired subframe values are shown in Figure 3 as normalized histograms alongside their fits to
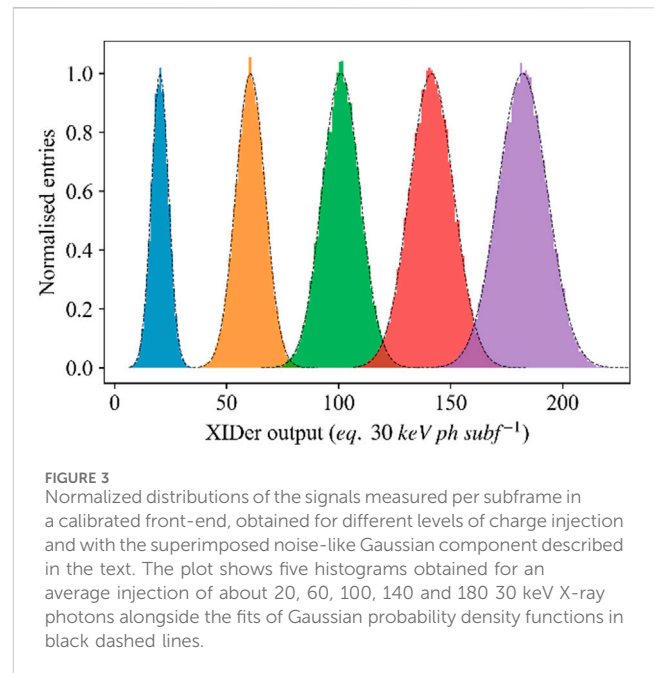


FIGURE 3
Normalized distributions of the signals measured per subframe in a calibrated front-end, obtained for different levels of charge injection and with the superimposed noise-like Gaussian component described in the text. The plot shows five histograms obtained for an average injection of about 20, 60, 100, 140 and 180 30 keV X-ray photons alongside the fits of Gaussian probability density functions in black dashed lines.

Gaussian functions plotted with dashed black lines. Qualitatively, the Gaussian shapes of the input charge distributions are properly retrieved by the front-end electronics, and the resulting distributions closely match their respective Gaussian fit, with no apparent defects. This is a neat indication of the consistency in the calibration of the front-end.

## 2.3 Photocurrent generation by LED illumination

The study of the response of semiconductor sensors to strong irradiation transients in the microsecond regime requires a readout system able to operate in such a time scale but also the possibility of modulating the incident photon flux with very short switching times, ideally shorter than the measurement intervals. When using X-rays, the very intense photon fluxes required for the measurements cannot be produced by conventional laboratory sources and the only option is to use pulsed beams from either X-ray free-electron lasers or from synchrotron radiation storage rings operating in timing modes. During the investigation of sensor response for the XIDer project, the limited availability of suitable beamtime as well as the lack of flexibility in selecting the time structure of the irradiation patterns with synchrotron beams has motivated the development of an alternative scheme to generate photocurrent time patterns using visible light.

The scheme implemented is the use of a 730 nm LED device mounted to produce a uniform illumination over the entire active surface of the sensor, and whose intensity and temporal structure can be modulated electronically. At this wavelength, the transmission of the light through a 20 nm thick platinum contact is close to 4% and the photon energy is above the bandgap of detector grade CdZnTe (1.57 eV, 790 nm) [37]. Therefore, a small but non-negligible part of the light can penetrate in the
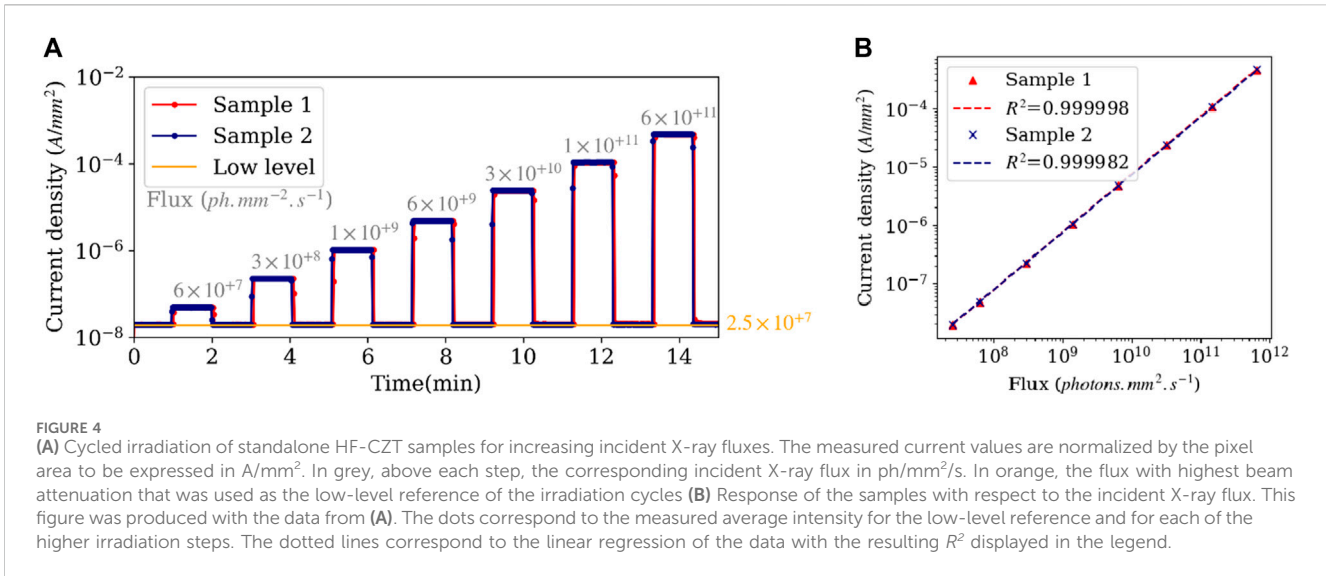
**FIGURE 4**
**(A)** Cycled irradiation of standalone HF-CZT samples for increasing incident X-ray fluxes. The measured current values are normalized by the pixel area to be expressed in A/mm². In grey, above each step, the corresponding incident X-ray flux in ph/mm²/s. In orange, the flux with highest beam attenuation that was used as the low-level reference of the irradiation cycles **(B)** Response of the samples with respect to the incident X-ray flux. This figure was produced with the data from **(A)**. The dots correspond to the measured average intensity for the low-level reference and for each of the higher irradiation steps. The dotted lines correspond to the linear regression of the data with the resulting $R^2$ displayed in the legend.

semiconductor material through the thin cathode metal and generate electron-hole pairs near the surface of the device, the absorption length of 730 nm light in CdTe being approximately 0.5 μm [38]. These conditions differ from the photocurrent generation by X-rays because of the different penetration depth. However, given that, at 20 keV, the attenuation length in Cd(Zn)Te is on the order of 80 μm, the absorption of X-rays in the low end of the energy range of interest can still be considered rather superficial when compared to the 1–2 mm thickness of the devices under study. Moreover, other observations made by the authors during preliminary measurements, although with not properly calibrated devices, have shown that the high-Z sensors have a similar response in stability measurements under LED illumination and under low-energy X-ray irradiation, as well as similar aftersignal time components. Those observations support our assumption that 730 nm LED illumination can appropriately emulate the illumination by superficially-absorbed low-energy X-rays.

## 3 Results

### 3.1 Linearity and stability of the HF-CZT standalone samples

The linearity and stability under quasi-static high-flux irradiation of the two standalone HF-CZT samples were investigated at the BM05 beamline of the ESRF. A multilayer monochromator was used to produce a 20 keV monochromatic X-ray beam reaching a maximum flux of $10^{12}$ ph/mm²/s on the samples. The beam was collimated to match the pixel size (500 μm × 500 μm) and aligned on one of the single pixels. The measurement consisted in subjecting the samples to 2-min long X-ray irradiation cycles with a progressively increasing maximum incident photon flux. A set of aluminum attenuators with 191 thickness combinations in steps of 60 μm was used to reduce the incident X-ray intensity and provide fast transitions between flux values. The attenuators could be changed remotely using a pneumatically-operated system with a response time of around 100 m.

The incident flux as a function of the number of filters was obtained prior to measuring the samples from the photocurrent measured in a 500 μm thick silicon photodiode inserted in the beam path. The lowest flux achievable with this setup, using 11.46 mm of aluminum, was $2.5 \times 10^7$ ph/mm²/s (in orange in Figure 4), and it was taken as the reference of the irradiation cycles. The samples were subjected to seven cycles with flux values ranging from $6\times10^7$ to $6 \times 10^{11}$ ph/mm²/s ($1.5\times10^7$ to $1.5\times10^{11}$ photons per pixel per second). Each cycle consisted of 1 minute of irradiation at a specific photon flux followed by 1 minute of irradiation at the low-level reference. During all the sequence, the photocurrent collected by the irradiated pixel was recorded every second using the picoammeter. As the irradiation sequences and the photocurrent measurements were not synchronized, there is usually one data point for each rising and falling edge that was measured during the change of attenuators. These data points are disregarded in the discussion. Figure 4A shows the measured current obtained for both standalone samples.

The two standalone devices exhibit similar behavior under cycled irradiation as well as an excellent linearity with the incident X-ray flux. This is depicted in Figure 4B, where the average measured intensity of the low-level reference and of each of the higher intensity irradiation steps are displayed as a function of the incident flux. In terms of stability, the rms variations of the measured photocurrent did not exceed the 0.4% of the mean value during the 1-min irradiation intervals, variations that are difficult to fully dissociate from the fluctuations of the intensity of the incident X-ray beam. Previous measurements, taken during longer intervals of 10 min, and for fluxes up to $10^{10}$ ph/mm²/s, have shown variations below 1 nA/mm² rms [31].

### 3.2 Transient response of HF-CZT standalone samples

The measurements in Figure 4A were not optimized to evaluate the transient response because the low-level reference did not correspond to the true dark current baseline and the recording
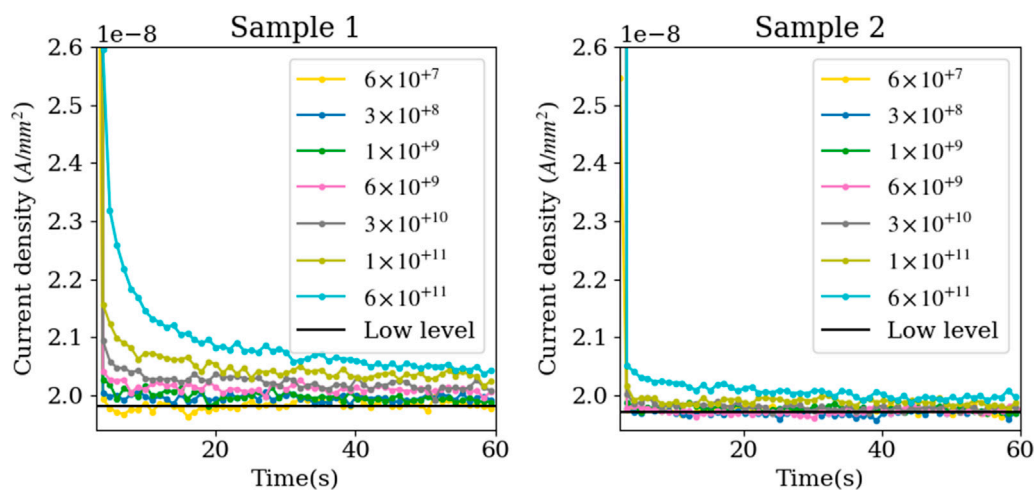
**FIGURE 5**
Zoom on the falling tails of the photocurrent steps presented in Figure 4A showing the aftersignal tails for sample 1 (left) and sample 2 (right). The flux values in the legends are given in ph/mm²/s. The black horizontal line represents the low-level reference that corresponds to an incident flux of 2.5 × $10^{+7}$ ph/mm²/s.

time resolution was limited to 1 s. However, these measurements still provide some useful information about the transient responses. Firstly, Figure 4A shows sharp rising edges for the pulses, regardless of the incident X-ray flux. Secondly, the falling edges exhibit some visible aftersignal, for instance after the last pulse of the sequence in the case of sample 1. The decay of the measured current for each sample is presented in more detail in Figure 5, in which the tails of the falling edges for all the irradiation levels are superimposed.

The data shown in Figure 5 gives a first insight into the aftersignal behavior of the sensors within the first 60 s after the end of the irradiation cycles. The aftersignal amplitude at a given time appears to increase with the incident X-ray intensity. In the case of sample 1, this behavior is clearly visible above $6 \times 10^9$ ph/mm²/s. In the case of sample 2, this behavior is only noticeable above $1 \times 10^{11}$ ph/mm²/s.

Before discussing these results further, another set of data, measured 1 year before the data shown in Figure 5, will be introduced to give more elements for the analysis. This older dataset, that is already published [31], comes from a similar measurement campaign, conducted with the same HF-CZT samples, at the same X-ray energy of 20 keV. However, there were some differences in the way the experiment was carried out. Firstly, the irradiation times were longer, 10 and 20 min for sample 1 and sample 2 respectively. Secondly, the low level of the cycles corresponded to the dark current baseline, which was about 100 pA/mm². This was feasible because the maximum flux used for those measurements, $8 \times 10^9$ ph/mm²/s, was two orders of magnitude lower than in the case of Figure 5, so that the strongest attenuation (using 11.46 mm of aluminum) corresponded to dark conditions. And finally, the photocurrent was sampled at a 4 Hz rate. In the Supplementary Figure S1 displays the photocurrent and aftersignal tails of both datasets side by side to facilitate the comparison between the two.

The superimposed tails of the current decay of the samples under cycled irradiation for the older dataset [31] are displayed in Figure 6. All the aftersignal values in the plots of the figure are the

result of subtracting the dark current component from the measured current.

The results of Figure 6 are similar for both samples. Aftersignal tails are visible and the aftersignal amplitude at a given time increases with the intensity of the preceding X-ray irradiation. The aftersignal presents a fast component, that cannot be measured with the low time resolution of this setup but is the subject of the following section, and a slow component with a decay time in the range of seconds. In order to illustrate the dependency of the slow component of the aftersignal with the irradiation, Figure 7 presents the levels observed in Figure 6 for both samples as a function of the photon flux. The values in Figure 7A are the aftersignal levels obtained 1 s and 60 s after the end of the irradiation cycle, while the chart in Figure 7B compares the aftersignal 1 s after the end of the irradiation with the average photocurrent measured during the irradiation interval.

The measured aftersignal tends to increase with the incident X-ray flux. The aftersignal values at 1 s for sample 2 are consistently smaller than for sample 1. However, this difference subsides, and is even reversed, for longer times. Even if the aftersignal amplitude increases with incident X-ray flux, the ratio between the aftersignal and the photocurrent produced during the irradiation phase remains small. After 1 s, this ratio is below 0.15%, even for the most intense irradiation conditions. And, after 60 s, the ratio drops below 0.01%.

Going back to Figure 5, we observe much larger aftersignal values for sample 1 than for sample 2. A possible explanation could lie in the difference of cathode contacts. Even if both gold and platinum act as electron blocking contacts, the Schottky barriers might react differently to the density of charge created by the irradiation near the cathode [21]. Following this line of thought, a medium-flux irradiation could introduce the small difference observed in the response of the samples in Figure 6 and Figure 7, and a high-flux irradiation would amplify this difference further, as observed in Figure 5. However, there is an alternative explanation for the large difference observed between samples in Figure 5, and it resides in the history of the samples. As
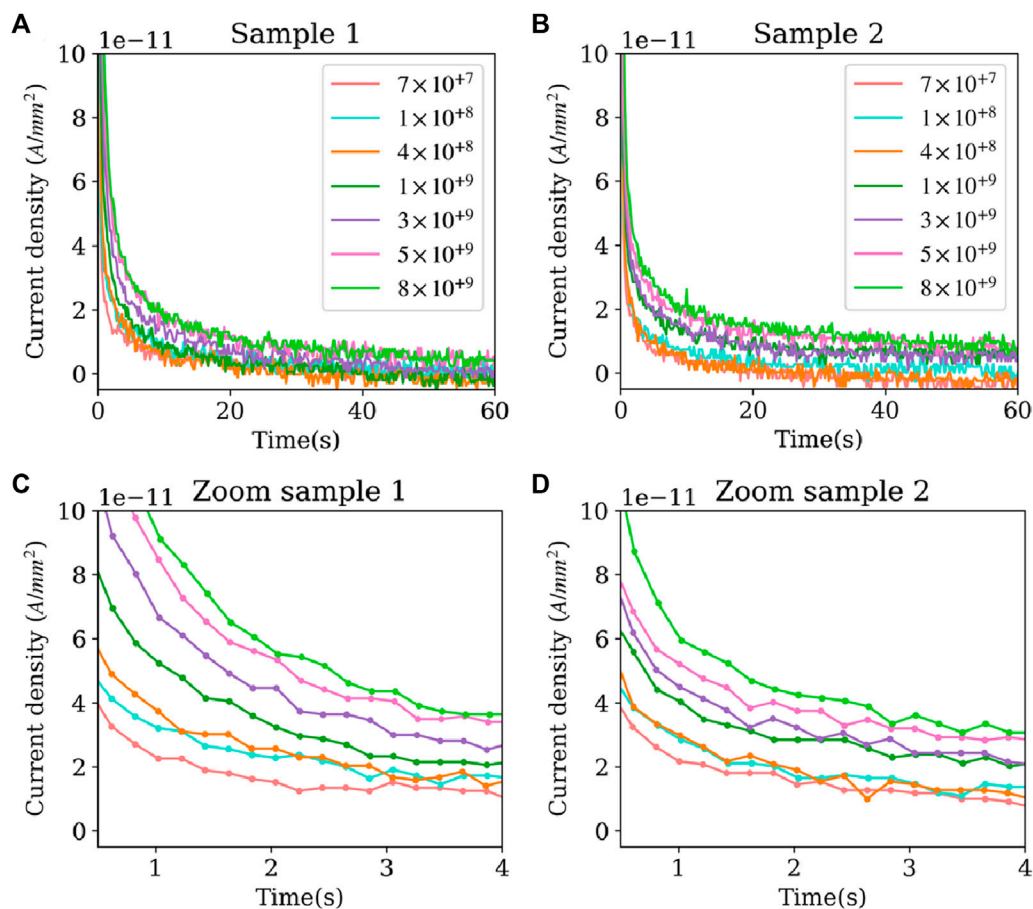
**FIGURE 6**
Baseline corrected aftersignal tails of the photocurrent measured in the two standalone HF-CZT samples after the cycled irradiation sequences described in [31] for different photon fluxes, in the legend, in ph/mm²/s. **(C)** and **(D)** are zoomed in plots of figure **(A)** and **(B)** respectively.
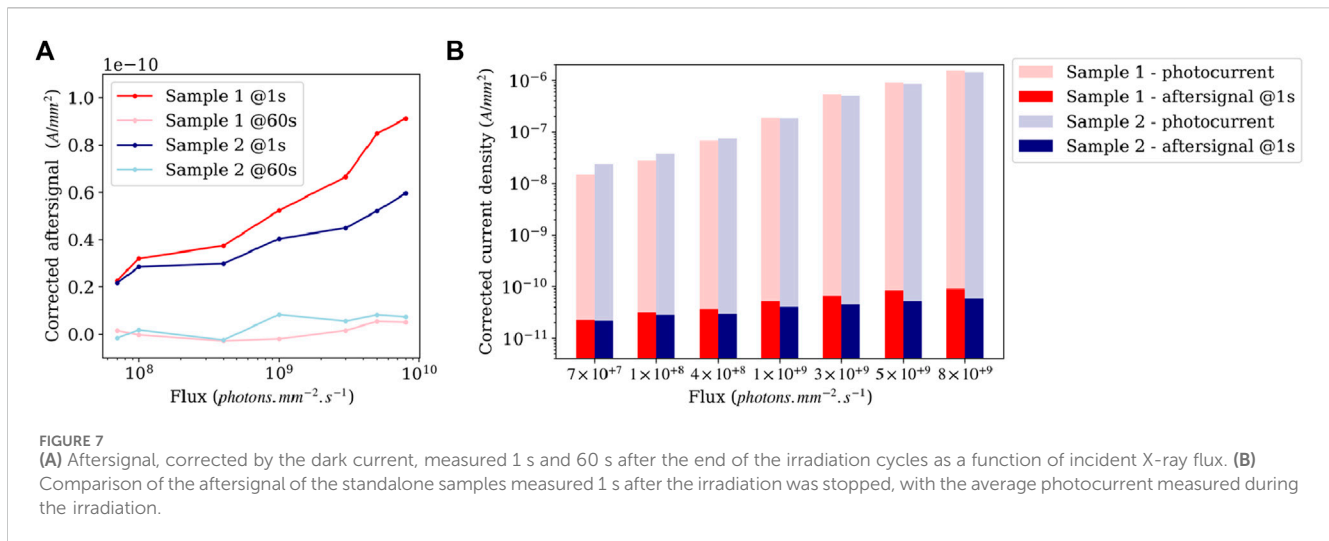
mentioned above, the dataset used in Figure 6 was measured 1 year prior to the one used in Figure 5. During this time period, sample 1 suffered an electrical breakdown on one of its corners. This corner was sanded down to remove the damaged part. Following this, the sensor remained functional but its transient response might have been affected by the introduction of new mechanically induced trapping centers. It is worth noting, however, that the preservation of the functionality of the sensor after such a crude removal of the damaged area can be taken as a strong indication of the resilience of the material.

To finish with, in Figure 5, no aftersignal is visible below $6 \times 10^9$ ph/mm²/s in the case of sample 1, and below $1 \times 10^{11}$ ph/mm²/s in the case of sample 2. This is due to a combination of two factors. Firstly, there is a significant difference between the transients observed in Figure 5 and those observed in Figure 6. On the one hand, in Figure 5, the transients correspond to the transition between a trapping-detrapping equilibrium at high flux and a trapping-detrapping equilibrium at a lower flux because, as previously mentioned, the low-level reference is not the dark current baseline. On the other hand, in Figure 6, the transients correspond to the transition between a trapping-detrapping equilibrium under high flux and the equilibrium under dark

conditions. This means that the trap states being emptied to reach equilibrium might not be the same, or at least, the concentration of traps emptied might not be the same. This could explain the faster transient response observed in Figure 5 compared with Figure 6 at similar incident X-ray fluxes. Secondly, because the low-level reference in Figure 5 is three orders of magnitude higher than the dark current baseline, the lowest picoammeter measurement range that could be used for the current measurement was 20 nA. This measurement range has an accuracy of 0.4%, so the smallest variations that could be recorded were $3 \times 10^{-10}$ A/mm². This is too large to measure any of the aftersignal responses observed in Figure 6.

## 3.3 Fast response of hybridized detectors

This section presents an example that illustrates the implementation of the methods introduced in Section 2 and their application to the evaluation of the fast components of the photocurrent aftersignal transients of HF-CZT and CdTe pixelated sensors. For this purpose, the following results were obtained from 200 µm pixel pitch devices connected to XIDer readout ASICs as described in 2.3 and the measurements were

**FIGURE 7**
**(A)** Aftersignal, corrected by the dark current, measured 1 s and 60 s after the end of the irradiation cycles as a function of incident X-ray flux. **(B)** Comparison of the aftersignal of the standalone samples measured 1 s after the irradiation was stopped, with the average photocurrent measured during the irradiation.

performed by illuminating the assemblies with LED light emulating low-energy X-rays as discussed in 2.4. As the XIDer devices were carefully pre-calibrated to provide the value of the integrated charge as an integer number of 30 keV equivalent photons, the adopted approach is to express the LED illumination also in the same units by assuming that under continuous illumination conditions, the readout values provided by XIDer are a good representation of the equivalent incident flux. This assumption would not be fully valid to provide accurate absolute flux values if the charge generation or the collection efficiency in the sensors is not ideal, but it can be taken as an adequate approximation to investigate the dynamic performance of the leakage current and the aftersignal effects. Therefore, despite the use of visible light, all intensity values for both incident and measured intensities in this example are referenced to 30 keV equivalent photons.
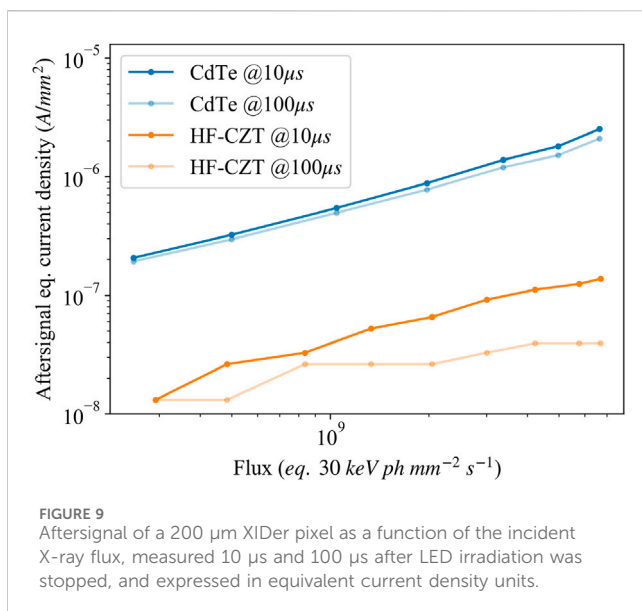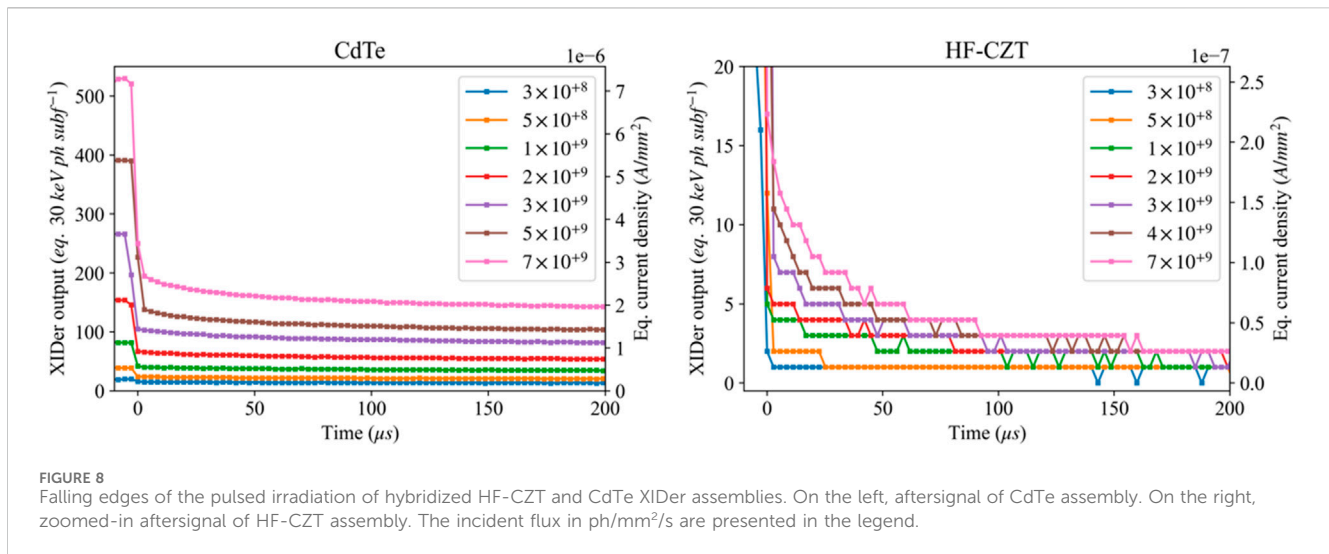
During the measurements, the assemblies were illuminated with a periodic 5 Hz square waveform of 50% duty cycle that corresponds to light pulses of 100 ms duration. The XIDer readout was set to acquire single subframes with a repetition period of 2.8 μs. This value is somehow arbitrary for the purposes of these measurement but it corresponds to the period of the orbit of the ESRF storage ring and is one of the standard subframe times foreseen for the regular final operation of XIDer at the ESRF. In the conditions of these measurements, the effective integration window within each 2.8 μs subframe period was of 1.97 μs, followed by a dead time of 0.83 μs. The LED source was independently characterized with a silicon photodiode to verify the proper shape of the light waveform and that the light emission fully decayed to zero in less than 1 μs at the falling edges of the illumination cycles.

Figure 8 shows the falling edges of the sensor current measured with the CdTe and HF-CZT assemblies under the pulsed illumination, for several light intensities ranging from 20 to 530 equivalent 30 keV photons per pixel per subframe. For the given pixel pitch and integration window, these values correspond to fluxes from $3\times10^8$ to $7 \times 10^9$ ph/mm²/s. The figure shows the response of one of the 200 μm pixels of each assembly once the steady state has been reached after several cycles of pulsed illumination. The plots present the pixel signal integrated for each 2.8 μs subframe during the time interval immediately following the falling edge of the incident illumination. They illustrate the level and temporal evolution of the aftersignal from the sensors. The vertical axis in the plot for the HF-CZT assembly has been expanded to reveal the aftersignal decay, as the measured values are between one and two orders of magnitude lower than in the case of CdTe. Because the subframe acquisition was not synchronized with the periodic 5 Hz illumination pulses, the first subframe recorded after the initial signal drop is likely to include partial illumination and should be disregarded.

The weaker HF-CZT aftersignals drop with a much smaller time constant when compared to CdTe. After a few hundred microseconds, the HF-CZT aftersignal integrated during one subframe drops below the 15 keV equivalent photon preset discrimination threshold, corresponding to half the least significant bit photon level, resulting in an effective null readout value. This coincidentally illustrates how the analog-to-digital conversion in the XIDer readout can completely discard residual signals by exploiting the intrinsic quantization of the X-ray illumination. This is the key feature of the incremental digital integration readout that makes possible in-pixel aggregation of multiple subframes without accumulating leakage current and similar undesired contributions, such the aftersignal, as long as they remain below the discrimination threshold.

The variation with the intensity of the illumination and the differences between sensor materials is more clearly appreciated in Figure 9, which presents the aftersignal level measured 10 and 100 μs after the end of the LED illumination pulses as a function of the injected signal expressed as equivalent X-ray flux. For comparison with the results in Figure 7, the measured aftersignal values in the vertical axis have been converted into equivalent current density units by using the pair creation energies tabulated in [13]. Please note again that the electric fields used for the standalone samples and the hybridized samples are different due to differences in thickness. This has to be considered when comparing the results from Figure 7, 9.

**FIGURE 8**
Falling edges of the pulsed irradiation of hybridized HF–CZT and CdTe XIDer assemblies. On the left, aftersignal of CdTe assembly. On the right, zoomed-in aftersignal of HF–CZT assembly. The incident flux in ph/mm$^2$/s are presented in the legend.



**FIGURE 9**
Aftersignal of a 200 μm XIDer pixel as a function of the incident X-ray flux, measured 10 μs and 100 μs after LED irradiation was stopped, and expressed in equivalent current density units.

## 4 Summary and outlook

This paper introduces the strategy followed at the ESRF for the development of 2D X-ray detectors suitable for experiments with the high brilliance beams produced by the last generation of synchrotron storage rings such as the ESRF-EBS source. The most demanding applications require charge-integrating detectors able to operate at high X-ray energies up to 100 keV and with photon fluxes that may reach $10^{11}$ ph/mm$^2$/s at the detector. A major challenge for building such a type of detectors is the proper management of the fluctuations and instabilities of the leakage current from the compound semiconductor sensors required to operate with high-energy X-rays. The presented approach is based on the use of the incremental digital integration readout scheme that is being developed within the XIDer project. This type of readout can mitigate the impact of sensor leakage current variations, as long they remain under certain limits [27, 28]. The availability of high-Z sensors with good performance under intense photon fluxes and

with low leakage current is therefore essential, and today, high-flux CZT is the only material candidate to fulfil those requirements.

The characterization of HF-CZT, in particular its ability to operate with high X-ray fluxes and the behavior of the leakage current is a crucial aspect. Understanding and quantifying the effects of the irradiation on the sensor performance including effects such as leakage or aftersignal variations are fundamental. The paper presents examples of the work recently started at the ESRF with HF-CZT sample sensors and some first promising results that confirm the much better performance of this material with respect to CdTe as it has already been observed under different conditions in several other published works [26]. The examples also illustrate how the XIDer readout can be used as a tool to evaluate the leakage variations in the micro- and sub-microsecond time scale. The results show good linearity and stability when the HF-CZT sensors are irradiated under quasi-static conditions with very high incident fluxes, well above $10^{11}$ ph/mm$^2$/s, showing no apparent drop in charge collection efficiency. The measurements also reveal the presence of weak but observable aftersignal components, i.e., a decaying residual current when the incident illumination on the sensor is sharply stopped or attenuated.

Our study is at an early stage, the measurements with HF-CZT have so far been performed at relatively low X-ray energies (20 keV) or with visible light illumination, conditions in which the charge carriers are generated close to the surface of the devices. An important aspect will be the investigation of the behavior of the HF-CZT sensors under higher-energy irradiation, up to 100 keV, which penetrates deeper into the material. A good understanding of all the dark or leakage components, not just the aftersignal, is essential. Some preliminary observations, still under investigation and that we plan to present in future publications, suggest an increase of the sensor leakage current that is induced by the irradiation itself, which adds to the generated photocurrent. If this effect is confirmed, the aftersignal component could be wholly or partly due to this additional leakage current component rather than only to charge detrapping processes in the sensor. Another important aspect that needs thorough study is the impact of the bias voltage and the operating temperature. So far, all the measurements have been carried out with HF-CZT sensors at room temperature. With the present knowledge of the leakage and charge

transport processes in these devices, it is difficult to predict the temperature dependence of the sensor response. However, it is not excluded that one could find operating conditions with significantly improved sensor performance.

Therefore, the deeper investigation of the HF-CZT sensors and a better understanding of their electro-optical response under high incident flux conditions is a key objective as it will have a decisive impact on the final design, construction, and operation of charge-integrating X-ray hybrid pixel detectors for high-energy applications with intense photon beams. In a more general way, the establishment by the detector community of a strong knowledge base on materials suitable for high-energy X-rays and high-flux applications is absolutely essential to overcome the challenges posed by the latest generation of synchrotron radiation sources. We expect that the ongoing work on the characterization of HF-CZT within the XIDer project will contribute in this direction.

## Data availability statement

The raw data supporting the conclusion of this article will be made available by the authors, without undue reservation.

## Author contributions

MC: Writing–original draft, Writing–review and editing, Conceptualization, Methodology, Visualization, Validation, Software, Formal analysis, Data curation, Investigation. OB: Writing–original draft, Writing–review and editing, Conceptualization, Methodology, Visualization, Validation, Software, Formal analysis, Data curation, Investigation. PB: Writing–review and editing, Funding acquisition, Project administration, Supervision, Resources, Conceptualization, Methodology, Visualization, Validation, Software, Investigation. PFa: Writing–original draft, Writing–review and editing, Funding acquisition, Project administration, Supervision, Conceptualization, Visualization, Validation. PFi: Writing–review and editing, Funding acquisition, Project administration, Supervision, Conceptualization. TM: Writing–review and editing, Funding acquisition, Project administration, Supervision. MRi: Writing–review and editing, Software, Resources. MRu: Writing–review and editing, Funding acquisition, Project administration, Supervision, Resources, Conceptualization, Methodology, Visualization, Validation. DS:

Writing–review and editing, Software, Resources. MW: Writing–review and editing, Methodology.

## Conflict of interest

Author MC, OB, PB, PFa, TM, MRu, and MW were employed by Detector and Electronics Group.

The remaining authors declare that the research was conducted in the absence of any commercial or financial relationships that could be construed as a potential conflict of interest.

## Publisher's note

All claims expressed in this article are solely those of the authors and do not necessarily represent those of their affiliated organizations, or those of the publisher, the editors and the reviewers. Any product that may be evaluated in this article, or claim that may be made by its manufacturer, is not guaranteed or endorsed by the publisher.

## Supplementary material

The Supplementary Material for this article can be found online at: https://www.frontiersin.org/articles/10.3389/fphy.2024.1304570/full#supplementary-material

## References

1. Susini J, Barrett R, Chavanne J, Fajardo P, Götz A, Revol JL, et al. New challenges in beamline instrumentation for the ESRF upgrade programme phase II. *J Synchrotron Rad* (2014) 21(5):986–95. doi:10.1107/S1600577514015951

2. Farvacque L. *EBS storage ring technical report*. France: ESRF (2018).

3. Raimondi P. ESRF-EBS: the extremely brilliant source project. *Synchrotron Radiat News* (2016) 29(6):8–15. doi:10.1080/08940886.2016.1244462

4. Rossi L, Fischer P, Rohe T, Wermes N. Pixel detectors: from fundamentals to applications. In: *Particle acceleration and detection*. Berlin, Heidelberg: Springer (2006). doi:10.1007/3-540-28333-1

5. Brönnimann C, Trüb P. Hybrid pixel photon counting X-ray detectors for synchrotron radiation. In: Jaeschke EJ, Khan S, Schneider JR, Hastings JB, editors. *Synchrotron light sources and free-electron lasers: accelerator Physics, instrumentation*

*and science applications*. Cham: Springer International Publishing (2020). p. 1191–223. doi:10.1007/978-3-030-23201-6_36

6. Ballabriga R, Blaj G, Campbell M, Fiederle M, Greiffenberg D, Heijne EHM, et al. Characterization of the Medipix3 pixel readout chip. *J Inst* (2011) 6(01):C01052. doi:10.1088/1748-0221/6/01/C01052

7. Maj P, Taguchi T, Nakaye Y. Tests of UFXC32k chip with CdTe pixel detector. *J Inst* (2018) 13(02):C02014. doi:10.1088/1748-0221/13/02/C02014

8. Donath T, Šišak Jung D, Burian M, Radicci V, Zambon P, Fitch AN, et al. EIGER2 hybrid-photon-counting X-ray detectors for advanced synchrotron diffraction experiments. *J Synchrotron Rad* (2023) 30(4):723–38. doi:10.1107/S160057752300454X

9. Medjoubi K, Hustache S, Picca F, Bérar JF, Boudet N, Bompard F, et al. Performance and Applications of the CdTe- and Si-XPAD3 photon counting 2D detector. *J Inst* (2011) 6(01):C01080. doi:10.1088/1748-0221/6/01/C01080

10. Tsigaridas S, Ponchut C. X-ray imaging with high-Z sensors for the ESRF-EBS Upgrade. *J Inst* (2019) 14(04):C04009. doi:10.1088/1748-0221/14/04/C04009

11. Becker W. Advanced time-correlated single photon counting techniques. In: *Springer series in chemical Physics*, 81. Berlin, Heidelberg: Springer (2005). doi:10.1007/3-540-28882-1

12. Loeliger T, Brönnimann C, Donath T, Schneebeli M, Schnyder R, Trüb P. The new PILATUS3 ASIC with instant retrigger capability. In: 2012 IEEE Nuclear Science Symposium and Medical Imaging Conference Record (NSS/MIC); October 29-November 3, 2012; Anaheim, California, USA (2012). p. 610–5. doi:10.1109/NSSMIC.2012.6551180

13. Andrä M, Dinapoli R, Bergamaschi A, Barten R, Brückner M, Chiriotti Alvarez S, et al. Towards MYTHEN 3: characterization of prototype chips. *Nucl Instr Methods Phys Res Section A: Acc Spectrometers, Detectors Associated Equipment* (2019) 936: 383–5. doi:10.1016/j.nima.2018.11.026

14. Grybos P, Kleczek R, Kmon P, Otfinowski P, Fajardo P, Magalhães D, et al. SPHIRD–Single photon counting pixel readout ASIC with pulse pile-up compensation methods. *IEEE Trans Circuits Syst* (2023) 70(9):3248–52. doi:10.1109/TCSII.2023.3267859

15. Magalhaes D, Fajardo P, Grybos P, Kleczek R, Ruat M. Very high rate X-ray photon counting 2D detectors with small pixels - the SPHIRD project. *IEEE NSS-MIC-RTSD Conf Proc* (2022). doi:10.1109/NSS/MIC44845.2022.10399295

16. Veale MC, Adkin P, Booker P, Coughlan J, French M, Hart M, et al. Characterisation of the high dynamic range Large Pixel Detector (LPD) and its use at X-ray free electron laser sources. *J Inst* (2017) 12(12):P12003. doi:10.1088/1748-0221/12/12/P12003

17. Allahgholi A, Becker J, Delfs A, Dinapoli R, Goettlicher P, Greiffenberg D, et al. The adaptive gain integrating pixel detector at the European XFEL. *J Synchrotron Rad* (2019) 26(1):74–82. doi:10.1107/S1600577518016077

18. Cline BD, Banks D, Bell S, Church I, Cross S, Davis A, et al. Characterisation of HEXITECMHz - a 1 MHz continuous frame rate spectroscopic X-ray imaging detector system. *Nucl Instr Methods Phys Res Section A: Acc Spectrometers, Detectors Associated Equipment* (2023) 1057:168718. doi:10.1016/j.nima.2023.168718

19. Grill R, Belas E, Franc J, Bugar M, Uxa Š, Moravec P, et al. Polarization study of defect structure of CdTe radiation detectors. *IEEE Trans Nucl Sci* (2011) 58(6):3172–81. doi:10.1109/TNS.2011.2165730

20. Cola A, Farella I. The polarization mechanism in CdTe Schottky detectors. *Appl Phys Lett* (2009) 94(10):102113. doi:10.1063/1.3099051

21. Cola A, Farella I. CdTe X-ray detectors under strong optical irradiation. *Appl Phys Lett* (2014) 105(20):203501. doi:10.1063/1.4902188

22. Ricq S, Glasser F, Garcin M. CdTe and CdZnTe detectors behavior in X-ray computed tomography conditions. *Nucl Instr Methods Phys Res Section A: Acc Spectrometers, Detectors Associated Equipment* (2000) 442(1):45–52. doi:10.1016/S0168-9002(99)01198-5

23. Overdick M, Baumer C, Engel KJ, Fink J, Herrmann C, Kruger H, et al. Status of direct conversion detectors for medical imaging with X-rays. *IEEE Trans Nucl Sci* (2009) 56(4):1800–9. doi:10.1109/TNS.2009.2025041

24. DECTRIS. *DECTRIS EIGER2 CdTe Technical specifications* (2018). Available: https://media.dectris.com/BR_EIGER2_X_CdTe_Jun2018_web.pdf (Accessed November 16, 2023).

25. Iniewski K. CZT sensors for Computed Tomography: from crystal growth to image quality. *J Inst* (2016) 11(12):C12034. doi:10.1088/1748-0221/11/12/C12034

26. Thomas B, Veale MC, Wilson MD, Seller P, Schneider A, Iniewski K. Characterisation of redlen high-flux CdZnTe. *J Inst* (2017) 12(12):C12045. doi:10.1088/1748-0221/12/12/C12045

27. Fajardo P, Busca P, Erdinger F, Fischer P, Ruat M, Schimansky D. Digital integration: a novel readout concept for XIDER, an X-ray detector for the next generation of synchrotron radiation sources. *J Inst* (2020) 15(01):C01040. doi:10.1088/1748-0221/15/01/C01040

28. Schimansky D, Busca P, Erdinger F, Fajardo P, Fischer P. Concepts for the XIDer readout ASIC incorporating a pipelined ADC with very low dead time. *J Inst* (2021) 16(03):P03023. doi:10.1088/1748-0221/16/03/P03023

29. Redlen. *Redlen Technologies website* (2023). Available: https://www.redlen.com/.

30. Koch-Mehrin KAL, Bugby SL, Lees JE, Veale MC, Wilson MD. Charge sharing and charge loss in high-flux capable pixelated CdZnTe detectors. *Sensors* (2021) 21(9): 3260. doi:10.3390/s21093260

31. Baussens O, Ponchut C, Ruat M, Bettelli M, Zanettini S, Zappettini A. Characterization of High-Flux CdZnTe with optimized electrodes for 4th generation synchrotrons. *J Inst* (2022) 17(11):C11008. doi:10.1088/1748-0221/17/11/C11008

32. Bettelli M, Zanettini S, Abbene L, Casoli F, Nasi L, Trevisi G, et al. High performance platinum contacts on high-flux CdZnTe detectors. *Sci Rep* (2023) 13(1):17963. Art. no. 1. doi:10.1038/s41598-023-45331-9

33. Polymer Assembly Technology. *Polymer assembly technology website* (2023). Available: https://www.polymerassemblytech.com/.

34. Clayton JE, Chen CMH, Cook WR, Harrison FA. Assembly technique for a fine-pitch, low-noise interface; Joining a CdZnTe pixel-array detector and custom VLSI chip with Au stud bumps and conductive epoxy. In: 2003 IEEE Nuclear Science Symposium. Conference Record; 19-25 October, 2003; Portland, Oregon, USA, 5 (2003). p. 3513–7. doi:10.1109/NSSMIC.2003.1352668

35. Acrorad. *Acrorad website* (2023). Available: https://www.acrorad.co.jp/index_en.html.

36. Collonge M, Busca P, Fajardo P, Williams M. Monte Carlo simulations for XIDer, a novel digital integration X-ray detector for the next generation of synchrotron radiation sources. *J Inst* (2022) 17(01):C01037. doi:10.1088/1748-0221/17/01/C01037

37. Owens A, Peacock A. Compound semiconductor radiation detectors. *Nucl Instr Methods Phys Res Section A: Acc Spectrometers, Detectors Associated Equipment* (2004) 531(1):18–37. doi:10.1016/j.nima.2004.05.071

38. Cola A, Farella I, Anni M, Martucci MC. Charge transients by variable wavelength optical pulses in CdTe nuclear detectors. *IEEE Trans Nucl Sci* (2012) 59(4):1569–74. doi:10.1109/TNS.2012.2194509